Utilising optimal general regression neural network (GRNN) inverse model for modelling and control of magnetorheological elastomer base isolation system

Abstract:

Magnetorheological elastomer (MRE) base isolations have attracted considerable attention over the last two decades thanks to its self-adaptability and high-authority controllability in semi-active control realm. Due to the inherent nonlinearity and hysteresis of the devices, it is challenging to obtain a reasonably complicated mathematical model to describe the inverse dynamics of MRE base isolators and hence to realise control synthesis of the MRE base isolation system. Two aims have been achieved in this paper: i) development of an inverse model for MRE base isolator based on optimal general regression neural network (GRNN); ii) numerical and experimental validation of a real-time semi-active controlled MRE base isolation system utilising LQR controller and GRNN inverse model. The superiority of GRNN inverse model lays in fewer input variables requirement, faster training process and prompt calculation response, which makes it suitable for online training and real-time control. The control system is integrated with a three-storey shear building model and control performance of the MRE base isolation system is compared with bare building, passive-on isolation system and passive-off isolation system. Testing results show that the proposed GRNN inverse model is able to reproduce desired control force accurately and the MRE base isolation system can effectively suppress the structural responses when compared to the passive isolation system.

Keyword: semi-active control; smart base isolation; magnetorheological elastomer; LQR; GRNN; fruit fly optimisation

1. Introduction

Magnetorheological elastomer (MRE) with magnetisable particles being dispersed in a rubber-like solid matrix (Deng and Gong, 2007), possesses changeable shear modulus that can be instantly controlled in a real time fashion through applying external magnetic field (Liao et al., 2012). Such unique feature has been widely utilised in research and development of MRE-based devices as semi-active controllable elements for vibration isolation in mechanical engineering, such as MRE based tuneable stiffness and damping vibration isolator (Liao et al., 2012), MRE seat suspension isolator with H∞ control (Du et al., 2011), engine vibration isolator (Alberdi-Muniain et al., 2013), etc. In civil engineering, the exploration of MRE base isolator for seismic protection of structures has also been carried out. Jung et al. (2011) conducted a conceptual investigation to explore the feasibility of utilising MRE's tuneable stiffness characteristics to improve the performance of conventional base isolation systems. Behrooz et al. (2014a) designed a variable stiffness and damping isolator (VSDI) with MR elastomer and achieved 39% increase on shear modulus. Li et al. (2013) designed a highly adjustable seismic base isolator with capacity to vary shear modulus up to 1600%. This base isolator, designed with a laminated structure of MRE and steel sheets, endows controllable shear flexibility while maintains high vertical stiffness that is essential for civil engineering applications. Some variation of this type of seismic isolators were also reported, such as a negative stiffness MRE base isolator (Yang et al. (2015)).

The successful development of MRE base isolation system has brought up an opportunity for great improvement of traditional base isolation systems, which currently is most widely used technique for seismic protection of civil engineering structures, including buildings and bridges. One of the key challenges to achieve such improvement lays on design and implement of real time feedback control of

MRE base isolation system utilising its controllable change of shear stiffness. For civil engineering applications, especially for seismic protections of structures, semi-active control is considered to be superior to both passive control and active control as it enables high authority control for high performance and flexibility as that of active control without compromising reliability and energy requirement (Yoshioka et al., 2002, Symans and Constantinou, 1999). However, the design of adequate semi-active controller to enable control effectiveness and efficiency imposes a challenge due to the nature of the semi-active control, i.e. the control action, which is also a function of the system status, can only be indirectly achieved by adjusting mechanical properties of semi-active devices such as stiffness or damping. On the other hand, most semi-active devices, such as MRF dampers or MRE isolators are known to be highly nonlinear and hysteretic by nature. A great deal of research efforts have been made to explore semi-active control of MRF dampers, such as modal based LQG controller (Wang and Dyke, 2013), Lyapunov-based control methods (Yi et al, 2001, Wang and Gordanienejad, 2002, Jansen et al., 2000), turbo-Lyaounov control (Cha and Agrawal, 2013), optimal control (Hiemenz et al. 2003). In comparison to MRF dampers, since research on real time control of MRE base isolation system is still at a conceptual and feasibility proof stage, there have been only limited control strategies explored for MR elastomer base isolation system (Behrooz et al., 2014b, Gu et al. 2016, Yang et al. 2015,). Different from MRF dampers or other semiactive devices, the principle of controlling MRE base isolators to protect structures is to produce instant motion decoupling between the harmful vibration source and the protected structures.

To control a structure equipped with semi-active devices, such as MRF dampers, the design of controllers often requires two stage actions in order to generate the required control: (i) determining the desired primary control action (such as actuation force) based on the feedback responses; (ii) determining required control command (i.e. the current/voltage) to drive the semi-active devices in order to generate primary control action (Xia, 2003). In other words, the control action required by the semi-active system relies on not feedbacks of the system but the inversed dynamics of the semi-active devices under a given status of the devices (i.e. instant displacements, velocities and accelerations).

When it comes to semiactive control approaches, a good demonstration is the clipped-optimal control (COC) proposed by Dyke et al. (1996) for real-time control of structures equipped with the MR dampers. In this control strategy, a simple clipped algorithm is used to generate the control command (zero or maximum voltage) to drive MR dampers based on the measured force feedback. The control strategy combines H_2/LQG optimal controller for calculating the desired control force and a voltage selecting algorithm for driving MR damper. In another word, two feedback loops are required: one for determining the desired control force from the system feedbacks and the other one for determining control commend (voltage to drive the devices) from the measured force feedback (Jansen and Dyke, 2000). There are two major drawbacks in these kinds of control strategies: firstly, the measurement of feedback actuation force might not be always feasible, e.g. in the case of MRE base isolator and secondly, the control efficiency is greatly compromised due to simple clipped control (zero or maximum). To this end, utilising inverse models that describes inverse dynamics between command signals and actuator force for determining control command to drive the device based on system feedbacks becomes popular in recent semi-active control research (Chang and Zhou, 2002; Bahar et al., 2010). However, due to inherent highly nonlinear and hysteretic nature of semi-active devices, it is not feasible to obtain explicit inverse dynamic model of semi-active devices. Taking advantage of neural network (NN) models in emulating arbitrary function at various accuracy levels (Cybenko, 1989),

several neural network based inverse models have been investigated for applications of MR dampers. Chang et al. (2002) explored the possibility of utilising the recurrent NN models to estimate the inverse dynamics of the MR dampers. Xia (2003) has developed an inverse model for MR damper utilising optimal multi-layer NN and system identification. Weber et al. (2014) utilised a neural network-trained inverse model of MR damper and applied the scheme on the vibration control of a five storey shear model. Askari et al. (2016) investigated an NN inverse model optimised by Takagi-Sugeno-Kang fuzzy scheme and such inverse model can well recurrent the desired control force However, inverse models published so far are complicated and unsuitable for real-time control applications. For example, they often require information not only at the present moment but also in previous time history (Xia, 2002, 2 historical time instants tracked; Weber et al., 2014, 4 historical time instants tracked; Askari, 2016, 5 variables with 3 historical time instants tracked each). The more retroactive information required, the longer inevitable delay tolerance will be produced. Some require a wide range of system inputs as training signal and extremely careful selection of regressor set. In addition, there is neither inverse model nor current selecting strategy being reported for real-time control of the MR elastomer base isolation systems.

To address the aforementioned challenges, this paper proposes a novel semi-active control for real-time feedback control of a MRE base isolation system. A classical LQR controller is selected as the primary controller to calculate desired control force based on the structural response. To generate the desired force, an inverse model based on general regression neural network (GRNN) is developed to determine the applied current to the MR elastomer isolator.

The main superiority of the proposed GRNN-based inverse model is summarised as follows:

- the model structure of GRNN-based inverse model is free of assumptions, which avoids complicated model identification.
- the proposed GRNN inverse model only requires inputs of displacement, velocity, force at present and one previous time instant, which will result in much less delay tolerance in the control.
- The GRNN adopts one-pass-learning algorithm which makes it much faster to form the conditional mean regression surface than commonly used back propagation (BP) algorithm, which is beneficial to online model training in the practical application.
- Different from other neural networks, the predictions of GRNN is always apt to converge to the global optimal solution and will not fall into the local optimum.
- The time interval from the calculation of optimal control force to the generation of the desired applied current is less than 1ms, satisfying the requirement of real-time structural control.

The proposed GRNN-based inverse model is developed using data from a prototype MRE base isolator (Li et al. (2013)). Experimentally identified dynamic characteristics of the MR elastomer isolator provide input-output data for the model training. The parameters of the inverse model are optimised by a fruit fly optimisation algorithm. The effectiveness of the proposed control method was testified both numerically and experimentally by implementing the MR elastomer base isolation system into a 3-storey building model. Approaches proposed by Gu et al. (2016) have been adopted to minimise the response time of the MRE isolator and hence realise the real-time control of the proposed system. Testing results show that the GRNN inverse model can effectively produce control command to

generate the desired control action. As a result, it offers effective real-time control to MRE base isolation system for significant reduction of the hazard caused by the devastating seismic events.

2. Prototype MRE base isolator and experimental characterisation for modelling

To utilise the unique features of MRE base isolator in semi-active control implementation, an inverse model which is able to accurately describe and reproduce the inverse dynamics of the MRE isolator has to be developed. The testing frame displayed in Figure 1 was designed and setup to acquire adequate MRE isolator's response data for the training of the inverse model taking advantages of the shake table in Civil Engineering Laboratory at University of Sydney, Technology.

The prototyped MRE isolator adopted in this study is designed by Li et al. (2013) The cylinder core of the isolator contains a laminated structure with 26 layers of 1-mm-thick MRE sheets and 25 layers of 1-mm-thick steel plates. The MRE sheets and steel plates are vulcanised together alternately. An electromagnetic coil is mounted around the core to generate magnetic field on MRE sheets according to the control current command. The annular gap between the core and coil allows a maximum ±15mm horizontal displacement of the isolator along all the directions. A dSPACE DS 1104 R&D controller board was employed as data acquisition system as well as command current controller. The A/D converter of dSPACE board consists of four 12-bit parallel channels and four 16-bit multiplexed channels. Three parallel channels were used to acquire the current, force and displacement signals, respectively. PWM output portal in slave DSP of dSPACE generates duty cycle signal to drive the current source according to the current control command. The PWM servo current drive was designed to minimise the response time of MRE isolator, of which details can be seen in the reference (Gu et al., 2015). As can be seen in Figure 1, the top plate of the isolator was connected to the reference wall via a Tedea Huntleigh C&T load cell (Part No. 0615-0200-G000-RS). The bottom plate of MRE isolator was fixed to the shake table, which provides horizontal motion for generating the deformation of the isolator. The displacement was measured by Baumer laser distance sensor (Part No. OADM 20I4460/S14C). The current input to the isolator was measured by a Hall Effect current transducer (Part No. CSLA2CD).

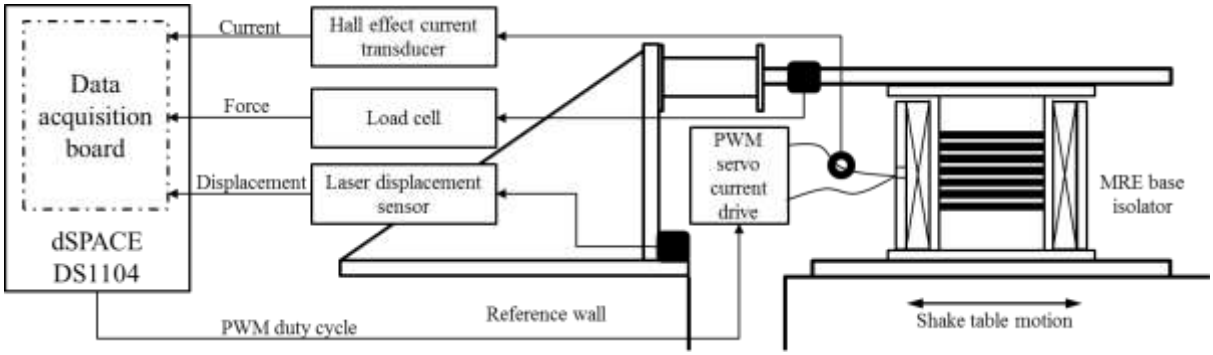

Figure 1 Experimental setup for MRE inverse model identification

Using experimental setup displayed in Figure 1, a series of tests has been conducted to observe the MRE isolator's dynamic response under various types of loadings. To obtain high quality trained inverse model, the training and testing data has to be selected carefully. In this study, the current signal was chosen to be a normally distributed random process within the range between 0A and 6A while the displacement signal was a sine sweep excitation with amplitude of 4mm and a frequency range from 0 to 4Hz. The data was sampled at a rate of 1000Hz for 35 seconds, which means 3,500 sets of data and

the first 30,000 sets were utilised as the training data and last 5000 sets were used as validation data. Loading signals of current and displacement as well as force response of MRE isolator are shown in Figure 2.

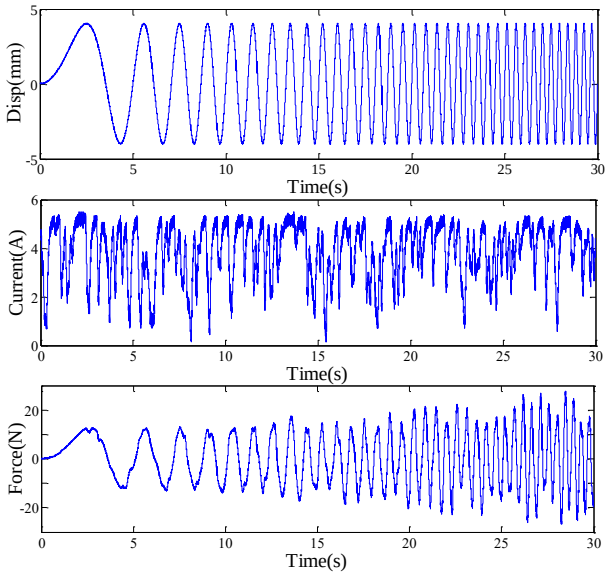

Figure 2 Training data for GRNN inverse model

3. Optimal GRNN inverse model of MRE base isolator

This section presents the development of the optimal inverse model of MRE base isolator. The methodology of general regression neural network (GRNN) is firstly introduced, followed by a fruit fly optimisation seeking for best smoothing factor σ in GRNN. In the third part, an inverse model based on optimal GRNN is developed and the accuracy of the proposed inverse model was testified by comparing the measured and predicted currents for MRE isolator.

1) General regression neural network (GRNN)

The general regression neural network (GRNN), proposed by Specht in 1991, is one type of radial basis function (RBF) network, which is used to set up the complicated regression between a group of independent variables X and the target output Y. It was developed based on nonlinear regression analysis. Suppose the joint probability density function (PDF) of random variables x and y is $f(x, y)$, if the observed value of x is X, the regression of X relative to y, i.e. conditional mean value, can be expressed as:

$$\hat{Y} = E\left(Y\middle|X\right) = \frac{\int_{-\infty}^{\infty} y \cdot f\left(X,y\right)dy}{\int_{-\infty}^{\infty} f\left(X,y\right)dy} \qquad \text{Eq. 1}$$

where X denotes the input and $\hat{Y}$ denotes the predicted output. If the PDF $f(x, y)$ is unknown, its non-parametric estimation can be obtained from the sample observations of x and y, shown as:

$$\hat{f}\left(X,Y\right) = \frac{1}{\left(2\pi\right)^{(m+1)/2}\sigma^{m+1}n}\sum_{i=1}^{n}\exp\left[-\frac{\left(X-X_i\right)^T\left(X-X_i\right)}{2\sigma^2}\right]\exp\left[-\frac{\left(Y-Y_i\right)^2}{2\sigma^2}\right] \qquad \text{Eq. 2}$$

where X_i and Y_i denote the sample observations of random variable x and y; σ is the smooth parameter that represents the width of the kernel function; n denotes the number of the samples; m denotes the dimension of random variable x. Substitute Eq. (2) for the PDF in Eq. (1) and the expression of expected conditional mean value of y given X is changed to the following equation:

$$\hat{Y}(X)=\frac{\sum_{i=1}^{n}\exp\left[-\frac{(X-X_i)^T(X-X_i)}{2\sigma^2}\right]\int_{-\infty}^{\infty}y\exp\left[-\frac{(Y-Y_i)^2}{2\sigma^2}\right]dy}{\sum_{i=1}^{n}\exp\left[-\frac{(X-X_i)^T(X-X_i)}{2\sigma^2}\right]\int_{-\infty}^{\infty}\exp\left[-\frac{(Y-Y_i)^2}{2\sigma^2}\right]dy} \quad \text{Eq. 3}$$

Here, a Euclid distance-based parameter is defined as

$$D_i^2=(X-X_i)^T(X-X_i) \quad \text{Eq. 4}$$

Due to the fact that $\int_{-\infty}^{\infty}ze^{-z^2}dz=0$, the expression of $\hat{Y}(X)$ is simplified via the integral operation, shown as:

$$\hat{Y}(X)=\frac{\sum_{i=1}^{n}Y_i\exp\left[-\frac{D_i}{2\sigma^2}\right]}{\sum_{i=1}^{n}\exp\left[-\frac{D_i}{2\sigma^2}\right]} \quad \text{Eq. 5}$$

In the GRNN, the smoothing factor σ is a key parameter, which directly affects the generalisation capacity of the trained network. When σ is assigned by a high value, $\hat{Y}(X)$ approximates the mean value of dependent variables of all the samples. However, when the value of σ tends to be 0, $\hat{Y}(X)$ will be close to the training samples. On this occasion, if the sample to be predicted is included in the training samples, the prediction is extremely close to corresponding dependent variable in the samples; otherwise, poor result will be obtained when the predicted sample is excluded from the training samples, which indicates the poor capacity of the network. Consequently, only when σ is appropriately set, the dependent variables of the training samples will all be considered in the calculation of output $\hat{Y}(X)$. Therefore, optimisation of smoothing factor σ has to be conducted for high quality GRNN. In this study, fruit fly optimisation algorithm (FOA) is employed to seek for best σ, which is illustrated in the following sections.

2) Fruit fly optimization algorithm (FOA)

FOA is a novel heuristic swarm optimisation algorithm with the benefits of few parameters, simple code implementation and easy adjustment. Based on the food search behaviour of fruit flies, the brief procedure of FOA can be summarised as the following steps.

Step 1. Initialise the position of the fly swarm: *X_axis* and *Y_axis*.

Step 2. Randomly assign the direction and range of each fly to search for food using the sense of smell:

$$X_i=X\_axis+RandomValue \quad \text{Eq. 6}$$

$$Y_i=Y\_axis+RandomValue \quad \text{Eq. 7}$$

where *RandomValue* denotes the search range.

Step 3. Because the actual position of food is unknown, the distance $Dist_i$ between the i^{th} fly and the original point (0,0) is calculated first. Then its reciprocal S_i, representing the smell concentration decision value of i^{th} fly, is obtained according to the following expression:

$$Dist_i = \sqrt{X_i^2 + Y_i^2} \quad \text{Eq. 8}$$

$$S_i = \frac{1}{Dist_i} \quad \text{Eq. 9}$$

Step 4. Substitute the value of S_i into the fitness function to get the smell concentration value of i^{th} fly:

$$Smell_i = function(S_i) \quad \text{Eq. 10}$$

Step 5. In the fruit fly swarm, find out the fly with minimum smell concentration value (for minimization optimisation problem):

$$[bestSmell \quad bestIndex] = \min(Smell_i) \quad \text{Eq. 11}$$

where *bestSmell* denotes the optimal concentration value and *bestIndex* denotes the index number of the fly with the optimal smell concentration.

Step 6. Preserve the coordinates of *x* and *y* as well as the best smell concentration *bestSmell*. In the meantime, the whole swarm will fly to this location according to the visual sense.

$$Smellbest = bestSmell \quad \text{Eq. 12}$$

$$X\_axis = X(bestIndex) \quad \text{Eq. 13}$$

$$Y\_axis = Y(bestIndex) \quad \text{Eq. 14}$$

Step 7. Iteratively repeat Step 2 to Step 5. Compare the current optimal smell concentrate with the previous one. If the current result is better than the previous one, conduct **Step 6**.

3) MRE base isolator inverse model based on FOA-optimised GRNN

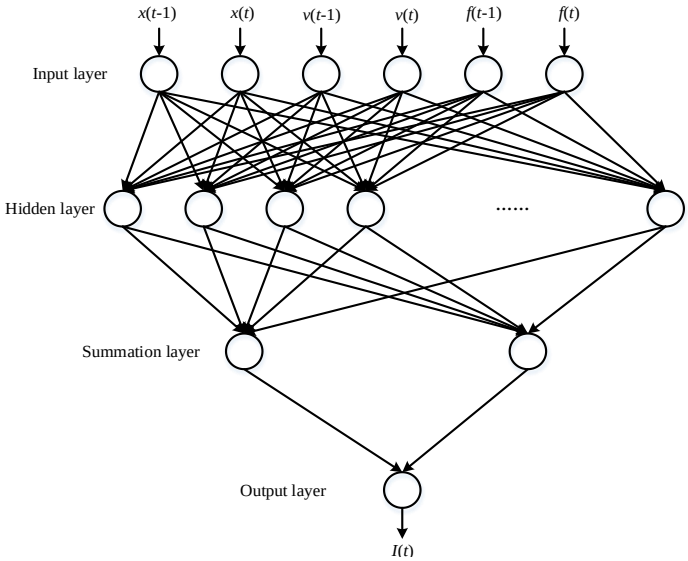

Figure 3 Configuration of GRNN-based inverse model for MRE isolator

A GRNN-based inverse model is built to depict the nonlinear relationship between device responses and applied currents. In this model, the input variables are displacement, velocity and shear forces captured at time t-1 and t while the output is the desirable applied current at time t. The configuration of the proposed inverse model of MRE isolator is shown in Figure 3, which consists of an input layer, a hidden layer, a summation layer and an output layer. The neuron number of input layer corresponds to the dimension of input variables and the function of input layer is to transmit these variables to next layer. In the hidden layer, each neuron corresponds to each training sample and the transfer function in this layer can be obtained from the denominator part in Eq. (5). Two sorts of neuron summations exist in the summation layer: one is the arithmetic summation and the other one is weighted summation. The neuron in the output layer corresponds to the current level that is supplied to the MRE isolator, which is equal to the ratio between two summations.

As aforementioned, smoothing factor plays an important role on the generalisation ability of trained network. Hence, to obtain the best prediction ability of the network, FOA is employed to select the best smoothing factor σ in GRNN. The detailed optimisation procedure is provided as follows:

i) Initialise the fruit fly swarm, including swarm size, maximum iteration number and initial positions. Here, the swarm size and maximum iteration number are set to be 20 and 100, as suggested by Pan et al. (2012). Because the food source is not known, each fly calculates the range between its position coordinate and original point according to Eq. (8), and then calculate the smell concentration according to Eq. (9).

ii) Replace the smoothing factor with the calculated smell concentration. Then, input the training samples and get the outputs of the network. For each fly, estimate its best individual fitness value and the best global fitness value of the whole swarm. Here, the fitness function is defined as the root mean square error (RMSE) between practical measured values and outputs of the GRNN, shown as:

$$function = \sqrt{\frac{1}{N}\sum_{i=1}^{N}\left[I_T(i) - I_0(i)\right]^2} \qquad \text{Eq. 15}$$

where N denotes the number of training samples; I_T and I_0 denote the practical measured currents and predicted currents from GRNN, respectively. The smaller the fitness value is, the better the obtained smoothing factor is. Store the fly with optimal fitness value and corresponding smell concentration in the swarm.

iii) Conduct the iteration procedure and repeat Steps 2-5 in Section 3.2. If the result at current iteration is superior to the previous best result, substitute the current best value for the previous one. This procedure will be terminated if the iteration number arrives at its maximum value.

The accuracy of the obtained inverse model is then demonstrated by comparing the measured current and model-predicted current in Figure 4(a). It can be clearly observed from Figure 4 that the optimal GRNN inverse model can precisely recurrent the inverse dynamics of the MRE base isolator. Moreover, Figure 4(b) provides the correlation coefficient R between experimental results and model outputs. The higher of this value is, the better the match between two types of responses is. Apparently, the optimal GRNN model can get the high value of R (0.9526), which satisfies the requirement in the modelling study. Accordingly, the proposed GRNN-based inverse model can be considered as a satisfactory solution to overcome the challenges in the semi-active control caused by high nonlinearity of the MRE base isolator and thus realise the vibration suppression control of isolated structures.

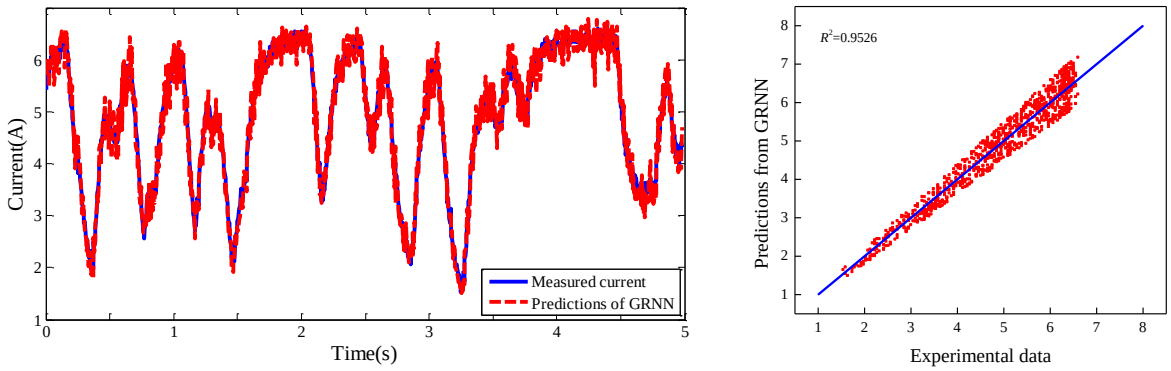

(a) (b)

Figure 4 Performance of the GRNN inverse model (a) comparison between measured current and GRNN output; (b) regression analysis of results

4) Comparison between GRNN inverse model and other inverse models

4. Control system of MRE base isolation system with GRNN inverse model

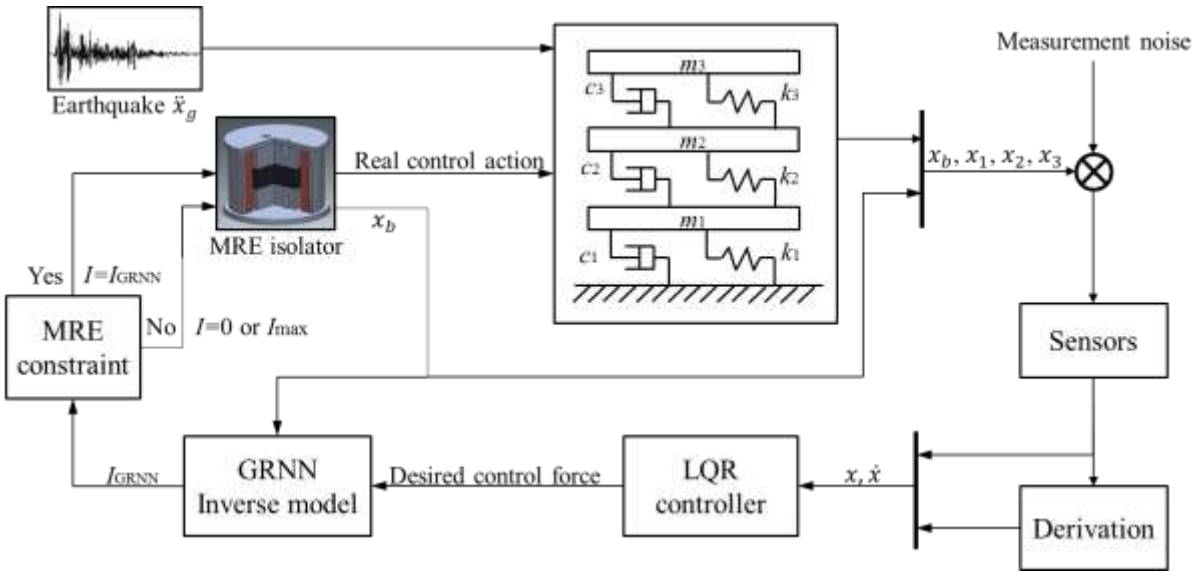

Figure 5 Semi-active control strategy of MRE base isolation system with GRNN inverse model

Figure 5 shows the control system of MRE base isolation system based on GRNN inverse model. Since LQR control algorithm is adopted in the primary controller, a full-state feedback is required to calculate the desired control force. The state vector $z = [x_b, x_1, \ldots, x_n, \dot{x}_b, \dot{x}_1, \ldots, \dot{x}_n]^{\mathrm{T}}$, in which x_b and $\dot{x}_b$ are the displacement and velocity of base level while x_i and $\dot{x}_i$ are the displacement and velocity of the ith level. After the calculation of optimal control force, the GRNN-based inverse model determines the current that has to be applied on the MRE base isolator to generate actual control force. Hence, the MRE base isolator can conduct control action indirectly by adapting itself to desired stiffness level according to the LQR control command. A strain-stiffening model developed by Yu et al. (2014) was utilised to simulate the dynamic behaviours of MRE base isolator, which can be written as

$$F(I,t) = k_b(I)\cdot x(t) + c_b(I)\cdot \dot{x}(t) + \alpha(I)\cdot x^3(t) \qquad \text{Eq. 16}$$

In which, the force generated by MRE isolator is a function of current I and time t; k_b and c_b are the stiffness and damping coefficient of MRE isolator, respectively; $x(t)$, $\dot{x}(t)$ and α are the base displacement, base velocity and strain-stiffening coefficient, respectively. The correlations between k_b, c_b and α and the current input I are expressed as following:

$$k_b(I) = 8.062 \cdot I + 4.523 \quad \text{Eq. 17}$$

$$c_b(I) = -0.0994 \cdot I^2 + 8.062 \cdot I + 4.523 \quad \text{Eq. 18}$$

$$\alpha(I) = -0.1232 \cdot I^2 + 0.7366 \cdot I + 0.007065 \quad \text{Eq. 19}$$

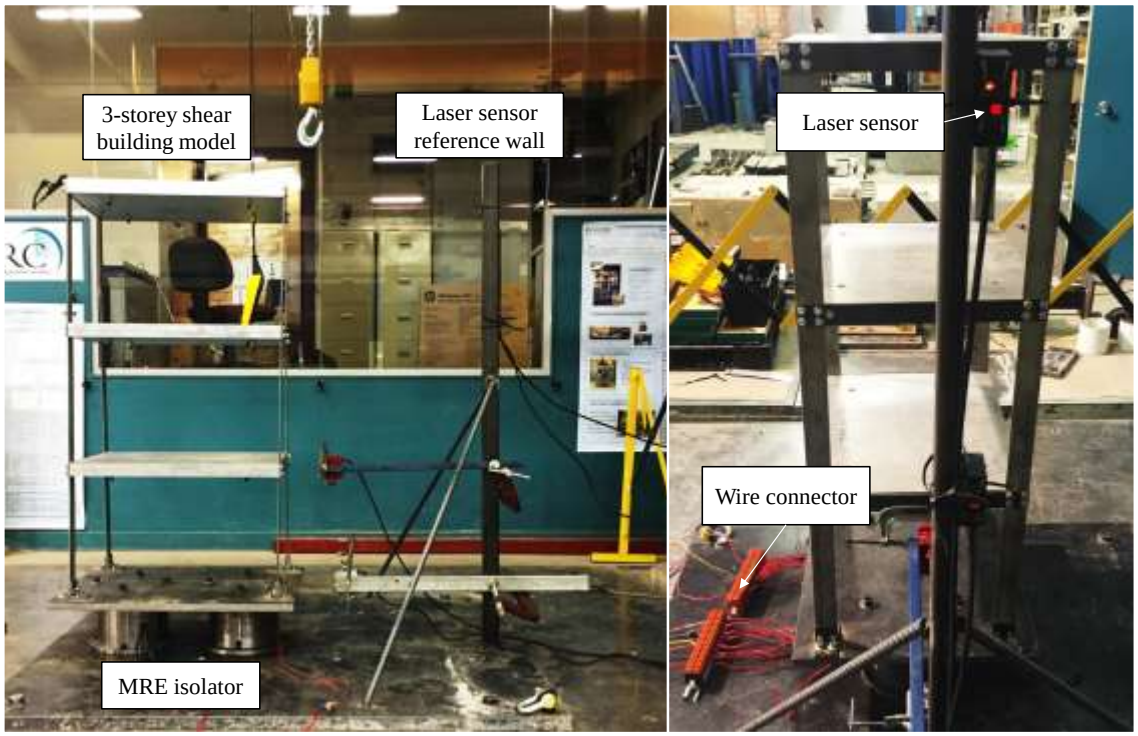

(a) (b)

Figure 6 Photo of the experimental setup of MRE base isolation system: (a) front view; (b) side view

The experimental setup of the MRE base isolation system is shown in Figure 6. As can be seen in Figure 6, the building model employed in this control system is a three-storey pure shear model. Therefore, it can be simplified to a 3-DOF lumped mass model, whose structural parameters have been summarised in Table 1. Two MRE isolators are mounted symmetrically under the 3-storey building model. Five Baumer laser distance sensors (Part No. OADM 20I4460/S14C) provide the measurements of shake table movement and relative displacement of each floor, x_g, x_b, x_1, x_2, x_3 (only four are used in the fixed base building case). A sensor reference wall is built to hold the laser sensors precisely at the elevation of each floor. A shake table is utilised to apply the designated earthquake excitation to the system accurately.

Table 1 Structural parameter of the three-storey building model

	Level 1	Level 2	Level 3
Mass (kg)	31.44	31.44	31.44
Stiffness (N·m)	20674.4	18545.1	21433.5
Damping (N·m/s)	7.63	6.42	5.61

5. Testing results and discussions

To demonstrate the effectiveness and versatility of the proposed MRE base isolation system, four benchmark earthquakes, namely, El Centro, Kobe, Hachinohe and Northridge earthquakes, have been applied on the isolated structure as the ground excitations. Four scenarios of the tested structure have been adopted, which are fixed base building, isolated building with passive-on MRE isolators (applied current = 3A), isolated building with passive-off MRE isolators (zero current input) and semi-active controlled MRE base isolator with the proposed control strategy.

Table 2 Comparative peak responses of experimental and numerical results

Earthquake	Isolation scenario	Peak inter-storey drift ratio		Peak floor acceleration		Peak relative displacement	
		Exp.	Num.	Exp.	Num.	Exp.	Num.
El Centro	Fixed base	11.32	10.48	0.28	0.22	28.90	26.91
	Passive-off	15.85	15.08	0.12	0.10	25.31	23.00
	Passive-on	5.61	5.33	0.15	0.11	18.53	18.42
	Controlled	4.94	4.66	0.13	0.11	15.69	8.95
Kobe	Fixed base	31.95	31.43	0.73	0.52	76.65	62.10
	Passive-off	60.77	58.33	0.45	0.41	95.94	60.88
	Passive-on	15.15	14.45	0.41	0.34	49.71	31.75
	Controlled	8.62	7.89	0.23	0.21	27.88	16.18
Hachinohe	Fixed base	4.77	4.42	0.12	0.10	11.90	9.38
	Passive-off	13.25	12.94	0.11	0.09	21.42	19.92
	Passive-on	4.62	4.22	0.09	0.07	11.12	9.71
	Controlled	2.18	2.14	0.05	0.04	6.76	6.47
Northridge	Fixed base	34.08	30.91	0.83	0.72	86.37	62.89
	Passive-off	31.42	29.00	0.30	0.27	53.23	45.22
	Passive-on	14.70	13.54	0.42	0.39	49.36	31.72
	Controlled	8.17	7.53	0.23	0.18	26.48	19.21

Figure 9 displays the top floor acceleration records of different isolation scenarios under four earthquakes. As can be seen from Figure 9, generally, any isolation strategy can achieve considerable acceleration attenuation effects when compared with fixed base structure. Moreover, the LQR control strategy with inverse model achieves the greatest acceleration reduction among three isolation scenarios. However, the passive isolation cases show little adaptability to the characteristics of earthquakes in that even both passive isolations perform well in El Centro and Kobe earthquakes, performances of the passive isolation systems need to be further improved under the other two earthquakes. Particularly, under Hachinohe earthquake, during several time periods, for instance, at around 4.5s, the acceleration response of the passive-off system even surpasses the fix-based building's response. Meanwhile, the passive-on isolation system performs better than the passive-off system under El Centro and Hachinohe earthquakes but its acceleration response is larger than that of the passive-off system under Kobe and Northridge earthquakes, which indicates that the designated passive-on isolation system may be more suitable for far-fault earthquakes while the passive-off system is more adaptable to the near-fault earthquakes.

To demonstrate the effectiveness of the proposed MRE base isolation system with GRNN inverse model and the feasibility of the system's practical application, both numerical and experimental testings have been conducted and compared on the MRE base isolation system. Given the horizontal deformation capacity of the MRE isolator, the magnitudes of all four earthquake accelerograms are all scaled by a factor of 15%. Figure 7 and Figure 8 display the comparative absolute top floor acceleration and relative base displacement of the system under four earthquakes. For better observability, the responses during typical 10 seconds (El Centro earthquake: 2~12s; Kobe earthquake: 5~15s; Hachinohe earthquake: 0~10s; Northridge earthquake: 2~12s) are illustrated in the graphs. As can be seen from Figure 7 and Figure 8, an ideal fitness between numerical and experimental responses is achieved. Nevertheless, the experimental results are slightly larger than the numerical ones around the local peaks.

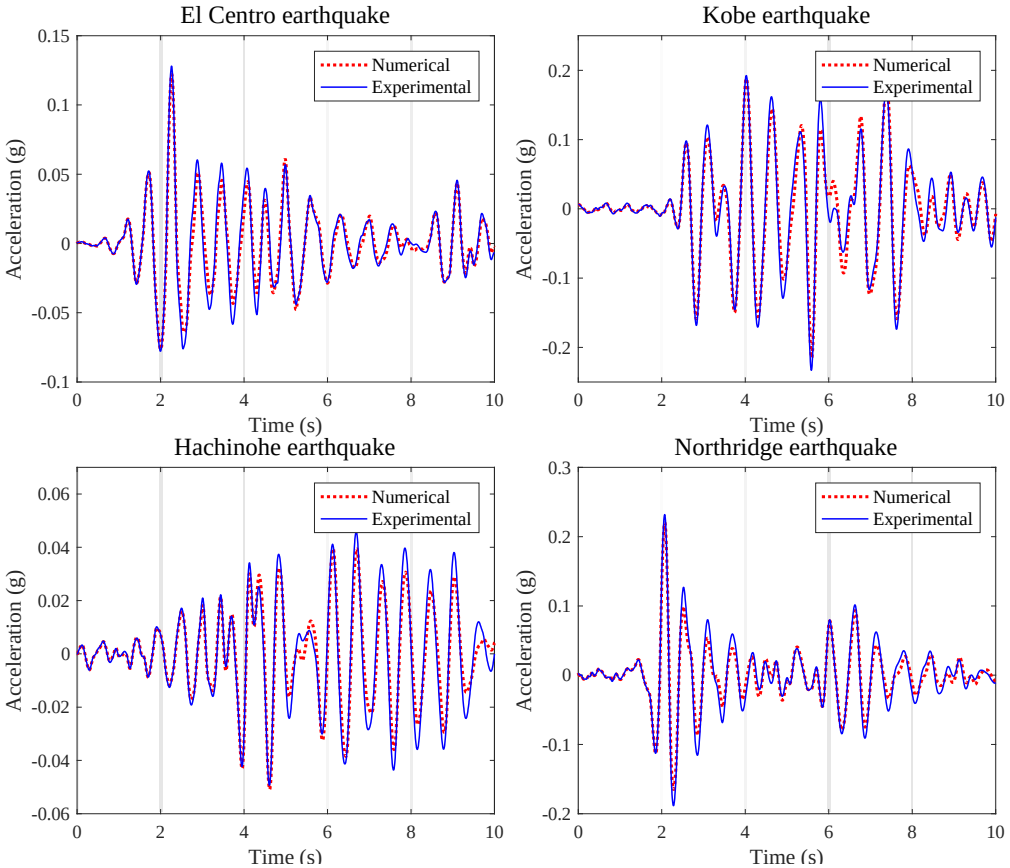

Figure 7 Experimental and numerical top floor accelerations of LQR controlled MRE base isolation system with GRNN inverse model

To further validate the numerical model, the numerical and experimental peak inter-storey drift, floor acceleration and relative displacement are compared in Table 2 under four earthquakes scaled by 15%. The peak responses of numerical and experimental results are fairly close with numerical slightly smaller than experimental under all conditions, which is consistent to the observation in Figure 7 and Figure 8. When compared with the fixed base scenario, both passive-on and LQR controlled isolation system can effectively reduce the structural responses in all three evaluative criteria under four earthquakes. In contrast, the passive-off system ends up in amplifying the inter-storey drift under all earthquakes but Northridge earthquake and relative displacement under Kobe and Hachinohe earthquakes. Among all the isolation system, the LQR controlled isolation system achieves smallest peak inter-storey drift, floor acceleration and relative displacement under all four earthquakes, which

indicates great effectiveness of the proposed isolation system in seismic response suppression performance.

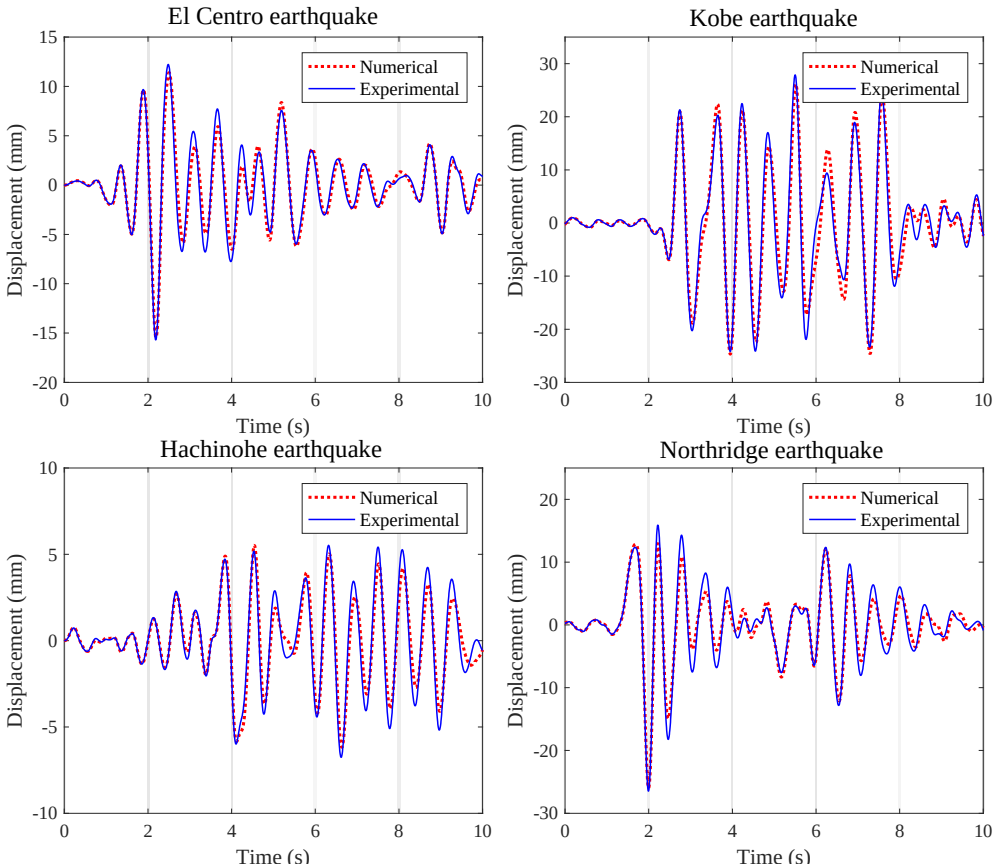

Figure 8 Experimental and numerical base displacements of LQR controlled MRE base isolation system with GRNN inverse model

Besides the top floor acceleration, the base displacement is also one of the criteria of great interest in the evaluation of the seismic protection performance of isolated structures since the common issue faced with the conventional isolation system is excessive base deformation which contributes to the failure of base isolators. Hence, Figure 10 compares the time histories of the four isolation scenarios under four earthquakes. It can be clearly observed from Figure 10 that, the passive-off system, due to the lowest lateral stiffness at base level, results in the poorest base displacement reduction performance under all earthquakes. As a matter of fact, except for Northridge earthquake, the peak base displacement of passive-off system surpasses that of the fixed base structure. The passive-on system achieves much better base displacement control performance than both fixed base building and passive-off system since the supplementary stiffness generated by applied current considerably increases the rigidity of the structure and hence increases the resistance to deformation at the base floor. However, such increase in rigidity may introduce undesirable acceleration to the structure as shown in Figure 9. Moreover, the LQR controlled system attains the most obvious reduction in base displacement. As can be seen from all the graphs in Figure 10, the LQR controlled base isolation system can not only reduce the peak value of the peak base displacement but also maintain the displacement at a relatively low level throughout the entire time history.

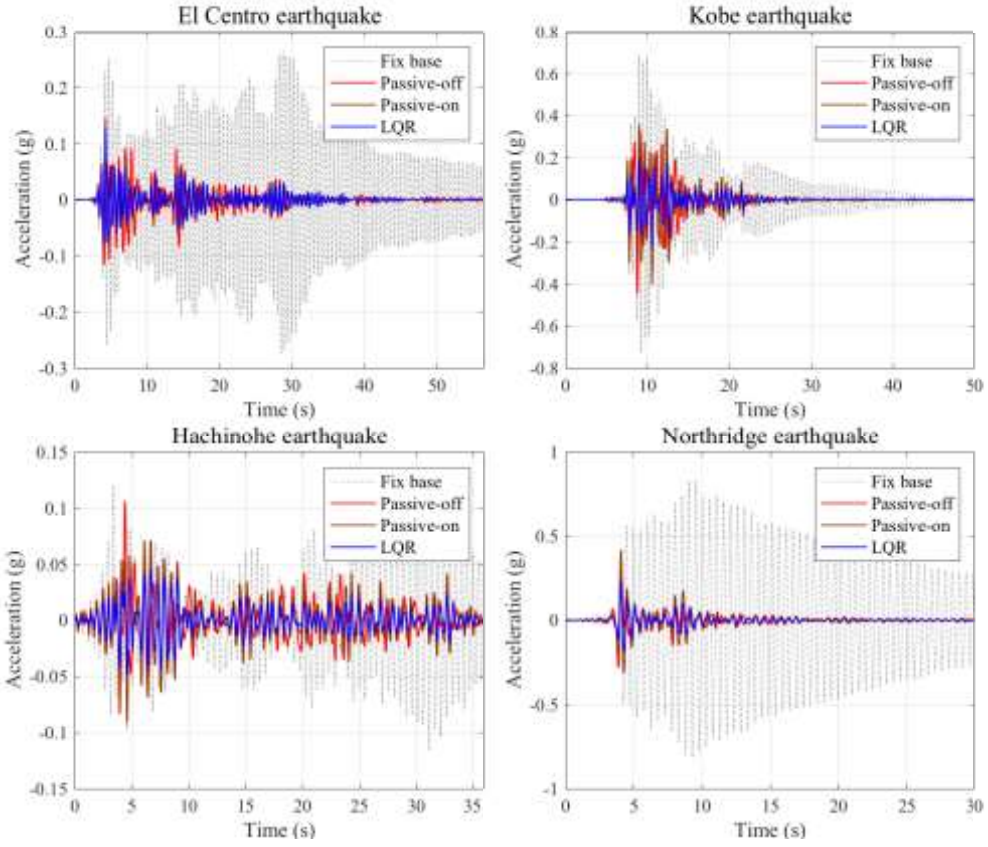

Figure 9 Time history of top acceleration with different isolation scenarios under four earthquakes

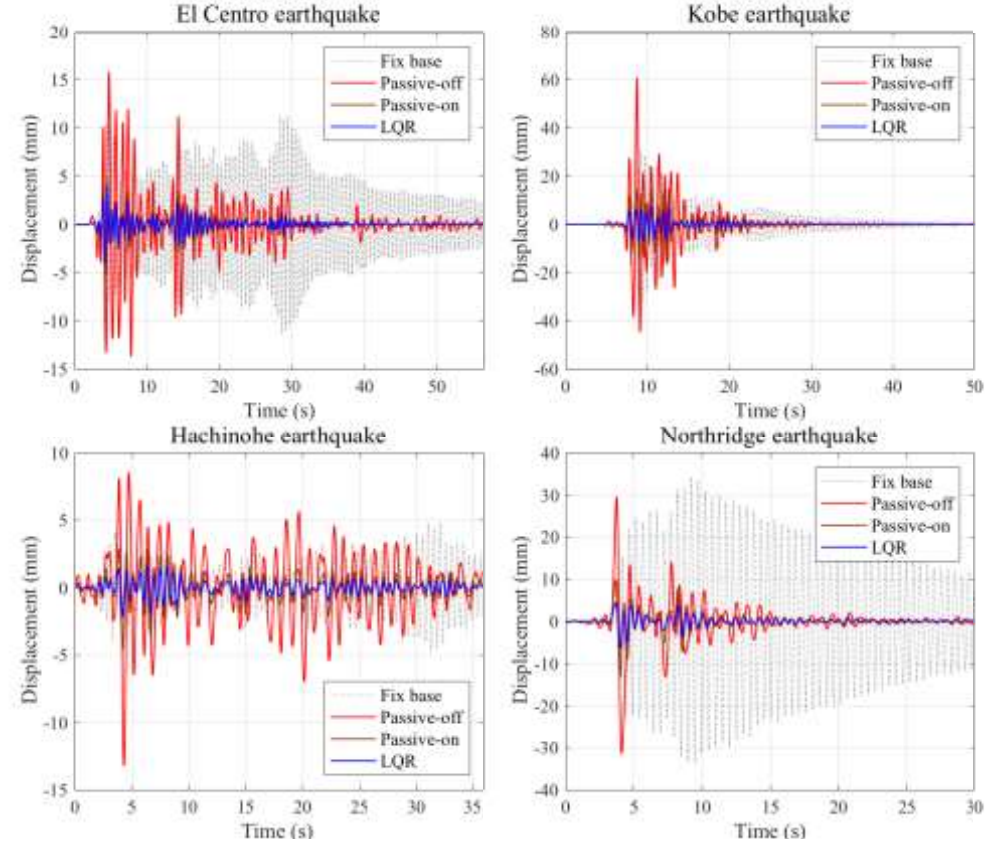

Figure 10 Time history of base displacement with different isolation scenarios under four earthquakes

Figure 11 to Figure 13 illustrates, the variations of peak value of inter-storey drift ratio, floor acceleration, relative displacement of the testing structure, in fixed base, passive-off isolation, passive-on isolation, and LQR controlled isolation scenarios and under four earthquake accelerograms. In Figure 11, inter-storey drift ratios are obtained by dividing peak inter-storey drift with the floor height of 400mm; floor accelerations are the peak acceleration at each level throughout the whole time history expressed in the term of gravitational acceleration *g*; displacements are the peak displacement relative to ground motion during the entire time history. The peak floor response of fixed base building is employed as the benchmark for protection effectiveness evaluation.

As can be seen from Figure 11, in the fixed building, the inter-storey drift ratio decreases as the structural height increases under all four earthquakes. Additionally, the inter-storey drifts of all three isolation scenarios are reduced, with respect to the fixed base building, on all levels except for the base level. The base inter-storey drift is actually equal to the base displacement and hence is not representative in the comparison of inter-storey drift. The base displacement of LQR controlled and passive-on systems are much smaller than that of the passive-off system, which is consistent to the observation of Figure 10. Except under El Centro earthquake, the LQR controlled isolation system achieves the smallest inter-storey drift ratio among all the isolation scenarios while under El Centro earthquake, its inter-storey drift is just slightly larger than that of the passive-off system on Floor 1 and 2. Moreover, the differences between inter-storey drift ratios of Floor 1~3 are not remarkable in all isolation systems, which indicates that the superstructure of isolated building approaches rigid body motion through concentrating structural flexibility in the base isolation floor.

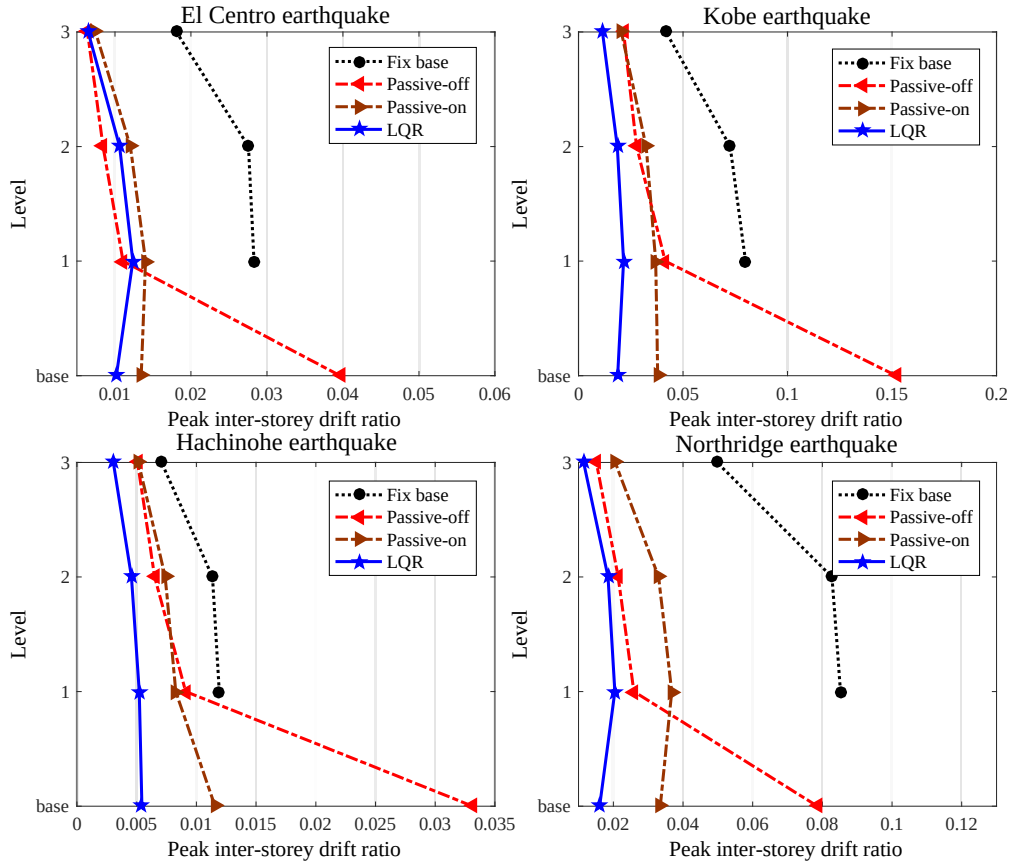

Figure 11 Peak inter-storey drift ratio (inter-storey drift/floor height (400mm)) of different isolation scenarios under four earthquakes

It can be observed from Figure 12 and Figure 13 that both peak floor acceleration and relative displacement increase along the elevation of testing structure in all isolation scenarios and under all earthquake accelerograms. The increase of acceleration and displacement along floor height side-proves that the first mode of the isolated structure is the major vibrational mode participating throughout all four seismic events. As for the peak floor acceleration suppression performance, it can be observed from Figure 12 that the LQR controlled isolation scenarios managed to significantly reduce the peak floor acceleration under different earthquakes at every storey unit. The passive isolation systems both perform well under all earthquakes except for Hachinohe earthquake, where the passive-off system's peak acceleration response outpaces the fixed base building by about 44% at the 1st floor and 5% at the 2nd floor while the passive-on system also slightly surpass the bare building at the 1st level.

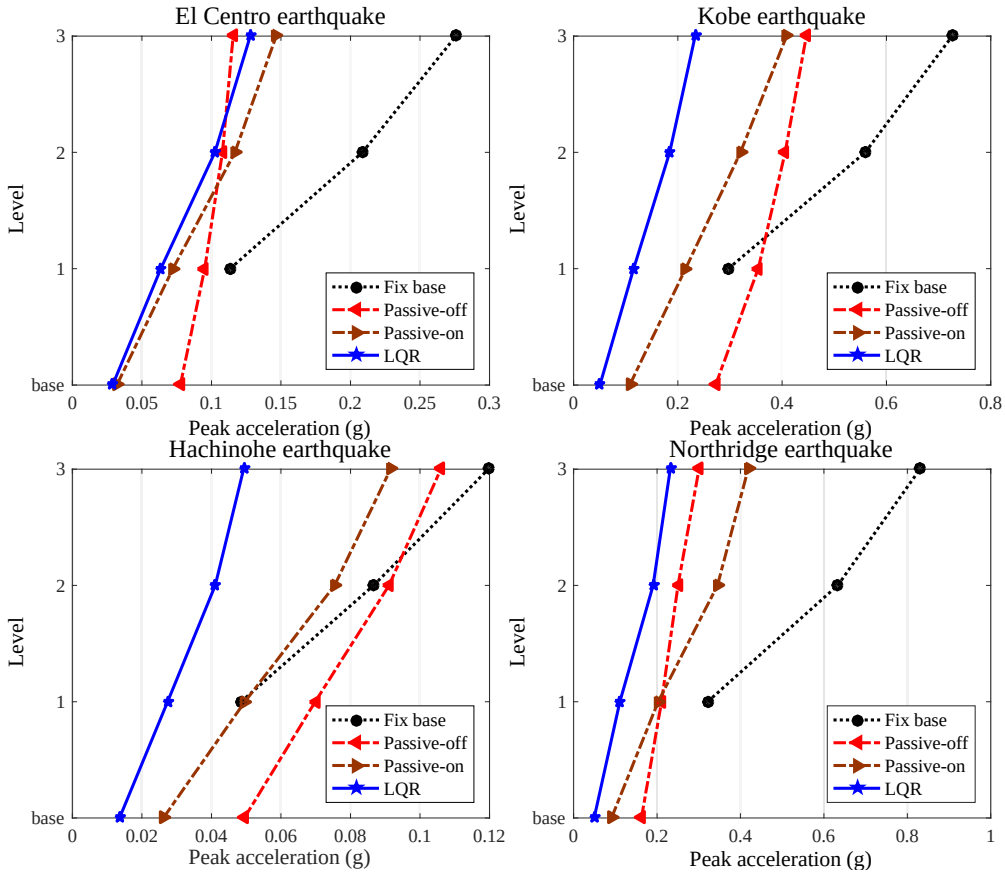

Figure 12 Peak floor acceleration of different isolation scenarios under four earthquakes

As for relative displacement, the passive isolation system shows a great reliance on the earthquake type in terms of suppression performance, i.e. under Kobe and Hachinohe earthquake, the passive-off isolation system's peak acceleration value is way larger than the fixed base building at all levels; under El Centro earthquake, the passive-off isolation system only realised reduction of 12% at the top value while under Northridge earthquake, the reduction is 29% at the 2nd floor and 38% at the top floor, respectively. The passive-on isolation system has a better performance but still enlarges the peak displacement by 57% under Hachinohe earthquake. With respect to the base displacement, the LQR controlled base isolation system receive the smallest peak base displacement under all accelerograms: 3.2mm under El Centro earthquake; 6.3mm under Kobe earthquake; 3.7mm under Hachinohe earthquake; 6.9mm under Northridge earthquake; which are all far less than the base displacements of passive isolation systems and fixed base building.

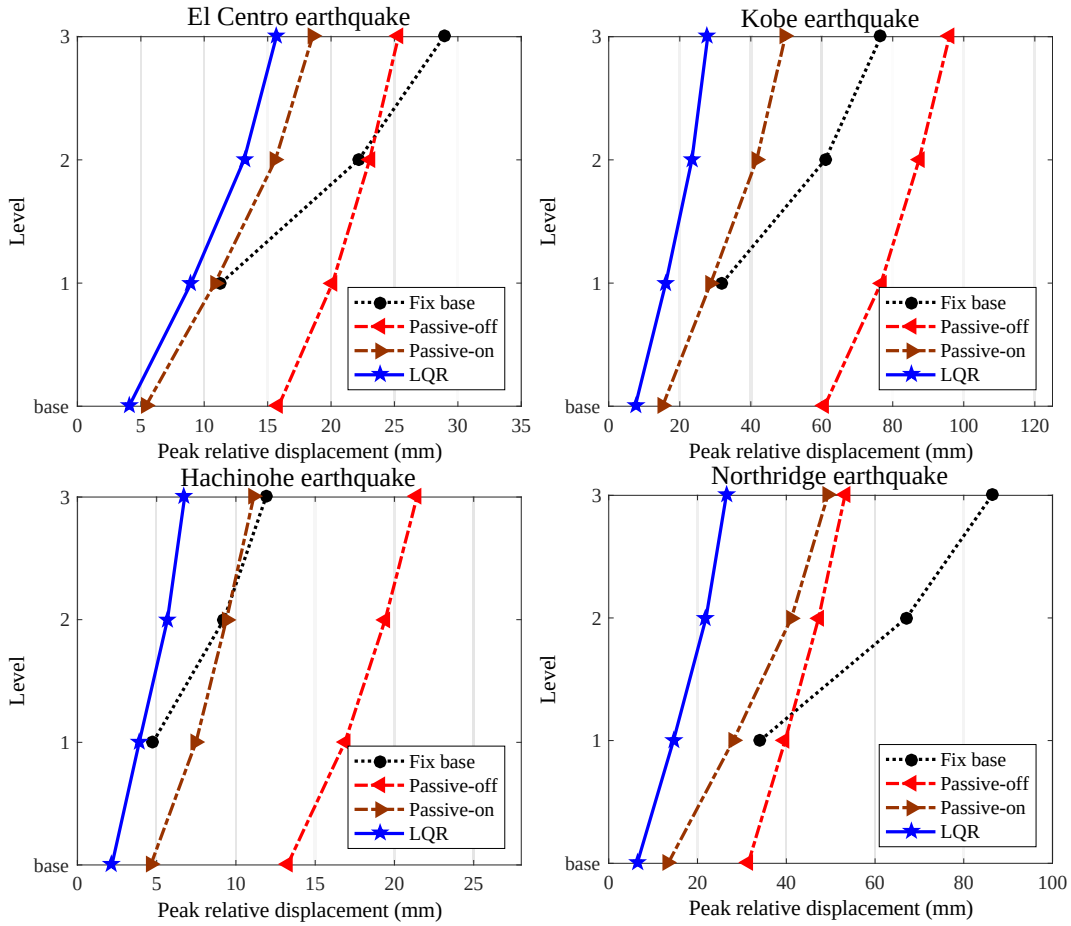

Figure 13 Peak relative displacement to ground motion of different isolation scenarios under four earthquakes

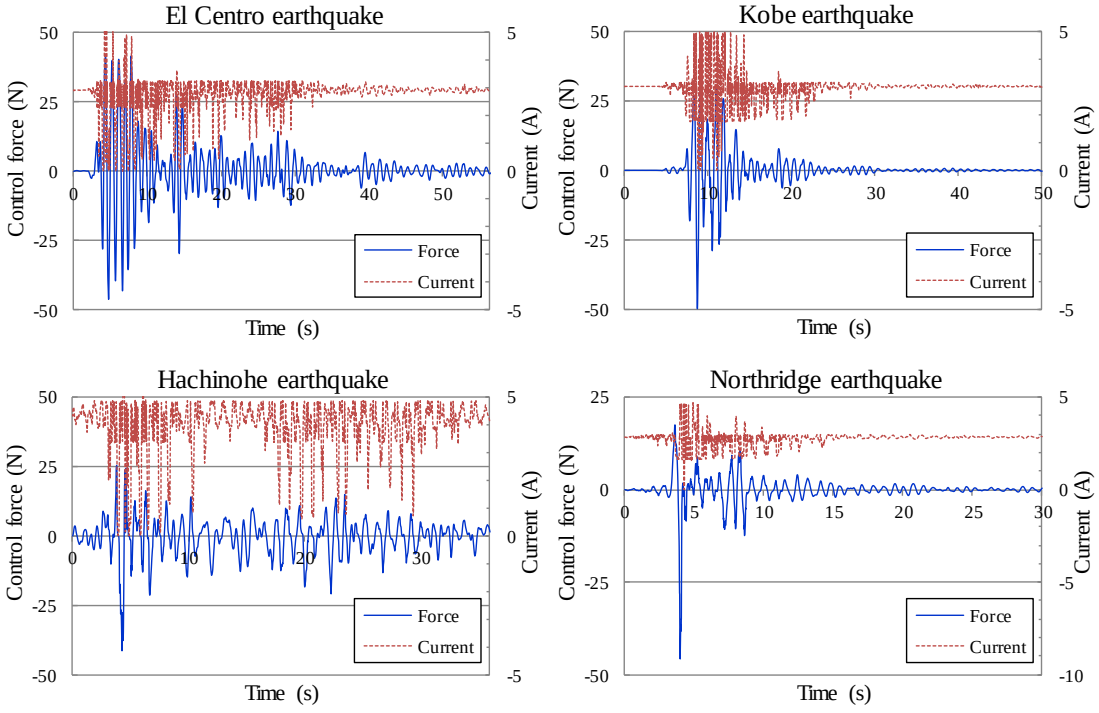

Figure 14 Time history of control force and corresponding control current of LQR controlled isolation system under four earthquakes

Figure 14 shows time histories of control force generated by the MRE isolator in LQR controlled MRE isolation system under four earthquakes. The corresponding control currents applied on the isolator to generate such control forces are also illustrated in Figure 14. Comparing the control current with the corresponding base displacement graph in Figure 10, it is discovered that the control current is retained at around 3A during most of the time but varies quite fiercely between 0 to 5A when the displacement is intense. In other words, when the external excitation is not dramatic, the LQR controlled isolation system behaves close to the passive-on system but when the seismic excitation causes excessive displacement, the LQR controller with inverse model generates current command that changes dramatically to control the performance of isolated structure. It is noteworthy that the control force shown in Figure 14 is the summation of control force generated by the two isolators in the MRE base isolation system. Meanwhile, Eq. 16 indicates that the control force is affected by not only applied current but also the deformation and velocity of the MRE isolator.

Five evaluative indices have been used to further evaluate the seismic protection performance, which assess the isolation structure's capability in reducing the peak and root mean square (RMS) of floor acceleration, peak and root mean square (RMS) of inter-storey drift and base shear. The indices can be expressed by Eq. 20 to Eq. 24.

$$J_1 = \frac{\max\limits_{i=1\sim4}\left\{\max\limits_{t}\left|\ddot{x}_i(t)\right|\right\}}{\ddot{x}^{\max}} \quad \text{Eq. 20}$$

$$J_2 = \frac{\max\limits_{i=1\sim4}\left\{\sqrt{\frac{1}{T}\sum \Delta t\cdot \ddot{x}_i^2(t)}\right\}}{\ddot{x}_{\max}^{RMS}} \quad \text{Eq. 21}$$

$$J_3 = \frac{\max\limits_{i=2\sim4}\left\{\max\limits_{t}\left|d_i(t)\right|\right\}}{d^{\max}} \quad \text{Eq. 22}$$

$$J_4 = \frac{\max\limits_{i=2\sim4}\left\{\sqrt{\frac{1}{T}\sum \Delta t\cdot d_i^2(t)}\right\}}{d^{RMS}} \quad \text{Eq. 23}$$

$$J_5 = \frac{\max\limits_{t}\left|\sum\limits_{i=1}^{4} m_i\ddot{x}_i(t)\right|}{F_b^{\max}} \quad \text{Eq. 24}$$

in which, $\ddot{x}_i(t)$, $d_i(t)$ and m_i are the acceleration, inter-storey drift and mass of the ith floor in the isolated structure; T is the total time; $\ddot{x}^{\max}$, $\ddot{x}_{\max}^{RMS}$, $d^{\max}$, d^{RMS} and $F_b^{\max}$ are the maximum acceleration, RMS of acceleration, maximum inter-storey drift, RMS of inter-storey drift and peak base shear of the fixed-base building. To compare the inter-storey drift in the superstructure, on the inter-storey drift at base floor (base displacement) is not taken into consideration in Eq. 22 and Eq. 23. The values of five evaluative indices are summarised in Table 3. Once again, the LQR controlled isolation system shows robust performance of vibration attenuation while the passive isolation systems' performances are closely relied on the external excitation. Meanwhile, the LQR controlled system has the smallest base shear among all three isolation systems, which shows such semi-active control system is able to achieve the best control performance by investing smallest control force.

Table 3 Evaluative indices under four earthquakes in different isolation scenarios

	Isolation scenarios	J_1	J_2	J_3	J_4	J_5
El Centro	Passive-off	42.85%	9.79%	0.47%	0.52%	76.1%
	Passive-on	53.57%	15.28%	1.50%	1.51%	65.9%
	LQR controlled	46.42%	5.10%	1.36%	1.43%	56.8%
Kobe	Passive-off	61.64%	8.38%	0.09%	0.03%	105%
	Passive-on	56.16%	12.67%	0.45%	0.16%	68.4%
	LQR controlled	31.51%	4.24%	0.59%	0.26%	39.1%
Hachinohe	Passive-off	91.67%	21.65%	2.92%	2.94%	143%
	Passive-on	75.00%	33.15%	1.96%	2.03%	102%
	LQR controlled	31.51%	11.26%	2.52%	2.84%	55.5%
Northridge	Passive-off	35.29%	12.13%	0.09%	0.08%	56.5%
	Passive-on	50.60%	18.60%	0.74%	0.68%	61.5%
	LQR controlled	27.71%	6.24%	1.03%	0.80%	33.4%

6. Conclusion

A semi-active controlled MRE base isolation system can apply control action indirectly by adjusting its own characteristics. To realise semi-active control of a MRE base isolation system, the inverse dynamics of a MRE base isolator has to be investigated to select current command properly according to the optimal control force. To this end, a control strategy based on LQR primary controller and optimal GRNN inverse model of MRE isolator has been investigated. The GRNN inverse network optimised by FOA speeds up training procedure by employing one-pass-learning strategy. The effectiveness of the proposed control strategy was validated numerically and experimentally by tests based on a three-storey building model under four benchmark earthquakes. Testing results demonstrate the superiority of the semi-active controlled base isolation system to passive-on and passive-off isolation systems in adaptability to various earthquakes as well as the capability of suppressing floor acceleration and inter-storey drift simultaneously. Such results indicate that the GRNN inverse model can effectively avoid the influence of highly nonlinear hysteresis of the semi-active device on the control system. Nevertheless, it was also discovered that the GRNN inverse model is a bit reluctant to track the desired control force when the rate of change is too large.

Reference

Alberdi-Muniain, A., Gil-Negrete, N. and Kari, L., 2013. "Modelling energy flow through magneto-sensitive vibration isolators. *International Journal of Engineering Science*," *65*: 22-39.

Askari, M., Li, J., Samali, B., & Gu, X. 2016. "Experimental forward and inverse modelling of magnetorheological dampers using an optimal Takagi–Sugeno–Kang fuzzy scheme". *Journal of Intelligent Material Systems and Structures, 27*(7), 904-914.

Bahar, A., Pozo, F., Acho, L., Rodellar, J. and Barbat, A., 2010. "Hierarchical semi-active control of base-isolated structures using a new inverse model of magnetorheological dampers". *Computers & structures*, 88(7): 483-496.

Behrooz, M., Wang, X. and Gordaninejad, F., 2014a. "Modeling of a new semi-active/passive magnetorheological elastomer isolator". *Smart Materials and Structures*, 23(4), p.045013.

Behrooz, M., Wang, X. and Gordaninejad, F., 2014b. "Performance of a new magnetorheological elastomer isolation system". *Smart Materials and Structures*," *23*(4):045014.

Chang, C.C. and Zhou, L., 2002. “Neural network emulation of inverse dynamics for a magnetorheological damper,” *Journal of Structural Engineering, 128*(2): 231-239.

Deng, H.X. and Gong, X.L., 2007. “Adaptive tuned vibration absorber based on magnetorheological elastomer. *Journal of intelligent material systems and structures*,” *18*(12):1205-1210.

Du, H., Li, W. and Zhang, N., 2011. “Semi-active variable stiffness vibration control of vehicle seat suspension using an MR elastomer isolator,” *Smart materials and structures, 20*(10): 105003.

Gu, X., Li, J., Li, Y. and Askari, M., 2016a. “Frequency control of smart base isolation system employing a novel adaptive magneto-rheological elastomer base isolator,” *Journal of Intelligent Material Systems and Structures*, *27*(7): 849-858.

Gu, X., Li, Y. and Li., 2016b. “Investigations on response time of magnetorheological elastomer isolator for real-time control implementation,” *Smart Materials and Structures*, 25(11).

Jansen, L.M. and Dyke, S.J., 2000. “Semiactive control strategies for MR dampers: comparative study,” *Journal of Engineering Mechanics*, 126(8): 795-803.

Jung, H.J., Eem, S.H., Jang, D.D. and Koo, J.H., 2011. “Seismic performance analysis of a smart base-isolation system considering dynamics of MR elastomers. *Journal of Intelligent Material Systems and Structures*,” *22*(13):1439-1450.

Li, Y., Li, J., Tian, T. and Li, W., 2013. “A highly adjustable magnetorheological elastomer base isolator for applications of real-time adaptive control.” *Smart Materials and Structures, 22*(9): 095020.

Liao, G.J., Gong, X.L., Xuan, S.H., Kang, C.J. and Zong, L.H., 2012. “Development of a real-time tunable stiffness and damping vibration isolator based on magnetorheological elastomer,” *Journal of Intelligent Material Systems and Structures, 23*(1): 25-33.

Pan, W.T., 2012. "A new fruit fly optimization algorithm: taking the financial distress model as an example," *Knowledge-Based Systems*, 26: 69-74.

Specht, Donald F., 1991. "A general regression neural network." *IEEE transactions on neural networks*, 2(6): 568-576.

Symans, M.D. and Constantinou, M.C., 1999. “Semi-active control systems for seismic protection of structures: a state-of-the-art review,’ *Engineering structures, 21*(6): 469-487.

Weber, F., Bhowmik, S., & Høgsberg, J. (2014). “Extended neural network‐based scheme for real‐time force tracking with magnetorheological dampers. *Structural Control and Health Monitoring*”, 21(2): 225-247.

Xia, P.Q., 2003. “An inverse model of MR damper using optimal neural network and system identification,” *Journal of Sound and Vibration, 266*(5): 1009-1023.

Yang, J., Sun, S., Tian, T., Li, W., Du, H., Alici, G. and Nakano, M., 2016. Development of a novel multi-layer MRE isolator for suppression of building vibrations under seismic events. *Mechanical Systems and Signal Processing, 70*, pp.811-820.

Yoshioka, H., Ramallo, J.C. and Spencer Jr, B.F., 2002. “Smart” base isolation strategies employing magnetorheological dampers. *Journal of engineering mechanics, 128*(5): 540-551.

Yu, Y., Li, Y. and Li, J., 2014. “Parameter identification of a novel strain stiffening model for magnetorheological elastomer base isolator utilizing enhanced particle swarm optimization,” *Journal of Intelligent Material Systems and Structures*, 1045389X14556166.

Yu, Y., Li, Y., Li, J., and Gu, X. 2016. "Self-adaptive step fruit fly algorithm optimized support vector regression model for dynamic response prediction of magnetorheological elastomer base isolator," *Neurocomputing*.